

1 *Supplement of*
2 **Using atmospheric observations to quantify annual biogenic carbon**
3 **dioxide fluxes on the Alaska North Slope**

4 Luke D. Schiferl, Jennifer D. Watts, Erik J. L. Larson, Kyle A. Arndt, Sébastien C. Biraud, Eugénie S.
5 Euskirchen, John M. Henderson, Kathryn McKain, Marikate E. Mountain, J. William Munger, Walter C.
6 Oechel, Colm Sweeney, Yonghong Yi, Donatella Zona, and Róisín Commane

7 *Correspondence to:* Luke D. Schiferl (schiferl@ldeo.columbia.edu)

8 **S1 Determining Tundra Vegetation Photosynthesis and Respiration Model (TVPRM) variable parameters using**
9 **observed net CO₂ flux**

10 The TPVRM variable parameters (α_s [units: $\mu\text{mol CO}_2 \text{ m}^{-2} \text{ s}^{-1} \text{ }^\circ\text{C}^{-1}$], β_s [$\mu\text{mol CO}_2 \text{ m}^{-2} \text{ s}^{-1}$], α_a [$\mu\text{mol CO}_2 \text{ m}^{-2} \text{ s}^{-1} \text{ }^\circ\text{C}^{-1}$], β_a
11 [$\mu\text{mol CO}_2 \text{ m}^{-2} \text{ s}^{-1}$], λ [$\mu\text{mol CO}_2 \text{ m}^{-2} \text{ s}^{-1} (\mu\text{mol photon m}^{-2} \text{ s}^{-1} \text{ mW m}^{-2} \text{ nm}^{-1} \text{ sr}^{-1})^{-1}$], and PAR_0 [$\mu\text{mol photon m}^{-2} \text{ s}^{-1}$] are
12 calculated for each 365-day period using a moving window (i.e., day 1–365, day 2–366, day 3–367, etc.) for 2013 to 2017 as
13 follows:

14 *Step 1: Linear regression of observed net CO₂ flux against soil temperature (T_s) to determine α_s and β_s and calculate*
15 *soil respiration (R_{soil}). Regression is performed on the median observed net CO₂ flux and T_s , determined by 5% bins of ordered*
16 *daily mean T_s and the corresponding daily mean observed net CO₂ flux, from the potential non-growing days (daily maximum*
17 *air temperature (T_a) $< 0^\circ\text{C}$) when SIF = 0 and 50% of the half-hours have observed net CO₂ flux.*

18 *Step 2: Linear regression of observed net CO₂ flux against T_a to determine α_a and β_a and calculate plant respiration*
19 *(R_{plant}). Regression is performed on the median observed net CO₂ flux with R_{soil} (calculated in step 1) removed and T_a ,*
20 *determined by 5% bins of ordered half-hourly T_a and the corresponding half-hourly observed net CO₂ flux with R_{soil} removed,*
21 *from the potential growing days (daily minimum $T_a > 0^\circ\text{C}$) when solar-induced chlorophyll fluorescence (SIF) > 0 and*
22 *photosynthetically active radiation (PAR) $\leq 4 \mu\text{mol photon m}^{-2} \text{ s}^{-1}$.*

23 *Step 3: Nonlinear fitting of observed net CO₂ flux against PAR, SIF, and T_a to determine λ and PAR_0 and calculate*
24 *gross primary productivity (GPP). Fitting is performed using nonlinear least squares (nls) on the half-hourly observed net CO₂*
25 *flux with R_{soil} and R_{plant} (calculated in steps 1 and 2, respectively) removed and half-hourly PAR, SIF (constant daily value)*
26 *and T_a (used to calculate the temperature scalar (T_{scale}) from the potential growing days when SIF > 0 and PAR $> 4 \mu\text{mol}$*
27 *photon $\text{m}^{-2} \text{ s}^{-1}$. Initial values for nls are $\text{PAR}_0 = 240$ and $\lambda = 0.04$.*

28 Each 365-day period must have valid data (observed net CO₂ flux, reanalyzed T_a , T_s and PAR, and derived SIF) for
29 70% of potential growing days and 50% of potential non-growing days in order for variable parameters to be calculated. This
30 requirement is most often failed due to gaps in the observed net CO₂ flux. In order to mitigate unrealistic observed non-growing
31 season uptake outside of noise, prior to step 1, we remove half-hourly observed net CO₂ flux values during 24-hour periods on

32 non-growing days when 50% of half-hours have observed net CO₂ flux and both 50% and the mean of those observed net CO₂
33 flux values are negative. For each step, data are removed when net CO₂ flux values are outside of three standard deviations of
34 the mean.

35 The moving window method accounts for variability in both day-to-day data availability and year-to-year ecosystem
36 response to environmental drivers (parameterization). The median value for each variable parameter from the set of valid 365-
37 day periods is used in the site-level net CO₂ flux evaluation and regional scaling. These median variable parameters are
38 determined for each combination of input reanalysis meteorology and SIF product at each eddy covariance flux tower site.

39 **S2 Meteorological reanalysis and other soil temperature products used by TVPRM**

40 Meteorological reanalysis products used by TPVRM are shown in Table S3. Downward shortwave radiation product (dswrf,
41 ssrd) values are converted to PAR using a conversion factor of 1.98. Meteorology values are linearly interpolated to half-
42 hourly (T_a, PAR) and averaged to daily (T_s) for model parameter calculation and site-level net CO₂ flux evaluation. NARR
43 values are linearly interpolated to hourly for regional simulations. Site-level calculations are made using values from the
44 meteorological product gridbox corresponding to site location. Meteorological product horizontal resolution is maintained for
45 regional simulations.

46 For TVPRM simulations driven by T_s from the Remote Sensing driven Permafrost Model (RS-PM (Yi et al., 2018,
47 2019)), we linearly interpolate RS-PM T_s from 8 day to daily values and horizontally regrid from 1 km to match the other
48 meteorological data by averaging all native pixel center points within each meteorological reanalysis product gridbox. When
49 sub-daily RS-PM T_s is needed to calculate the simulated net CO₂ flux, we apply a constant value. We tested the use of all RS-
50 PM T_s depths from 1 cm to 105 cm and found varying performance, with T_s from deeper layers improving the TVPRM
51 performance at sites with greater soil thickness. For consistent comparison to NARR, we use RS-PM T_s at 8 cm depth in our
52 analysis here.

53 We also tested using multi-layer fit driven by soil column temperature. In this approach, we summed the degrees
54 above a freezing threshold (-0.75°C at IVO, -5°C at CMDL) representing the zero-curtain time period for each layer, multiplied
55 by the layer thickness. This column sum temperature above freezing was used in place of the single layer T_s above in the same
56 linear fit process to determine parameters which represent R_{soil}. While likely more realistic in driving R_{soil} than a single layer
57 approach, applying the multi-layer sum to our constrained TVPRM member did not result in significantly higher early cold
58 season (Sep–Dec) CO₂ emissions needed to match the observations since both cases match well to the eddy flux measurements.

59 **S3 SIF products used by TVPRM**

60 SIF products used by TPVRM are shown in Table S4. GOSIF and CSIF are linearly interpolated to daily values and
61 horizontally regridded by averaging all native pixel center points within each meteorological reanalysis product gridbox. Any

62 resulting negative values for all products are set to 0. Site-level SIF values correspond to the site latitude (GOME-2) or site
63 location within a meteorology gridbox (GOSIF, CSIF). Regional simulation GOME-2 values correspond to the meteorology
64 gridbox center point latitude.

65 **S4 Evaluation of site-level net CO₂ flux against observations**

66 We calculate the TVPRM net CO₂ flux at half-hourly time resolution using the median variable parameters determined above
67 for each eddy flux site for each combination of reanalysis meteorology and SIF product. We then evaluate the simulated net
68 CO₂ flux against the observed net CO₂ flux for each eddy flux site over various averaging lengths (half-hour, one day, two
69 weeks) for various timeframes (year-round, growing season, non-growing season). Elements of this evaluation are shown in
70 Fig. S4. For this evaluation, we calculated the coefficient of determination (R^2) as the square of the Pearson correlation
71 coefficient for all points. The slope (m) is determined by ordinary least squares using the median of each 10% bin of ordered
72 observed and corresponding simulated net CO₂ flux. The normalized mean bias (NMB) of all points is defined as
73 $\frac{\sum(\text{simulated} - \text{observed})}{\sum \text{observed}}$. The root-mean-square error (RMSE) of all points is defined as $\sqrt{(\text{simulated} - \text{observed})^2}$.

74 Generally, site-level TVPRM performance is greater (higher correlation, slope closer to 1, lower bias and error) in
75 the growing season compared to the non-growing season. Performance improves in all seasons as the timescale of averaging
76 is lengthened, with the non-growing season notably better on the two-week scale, as soil temperatures do not fluctuate much
77 on the half-hourly to daily scale.

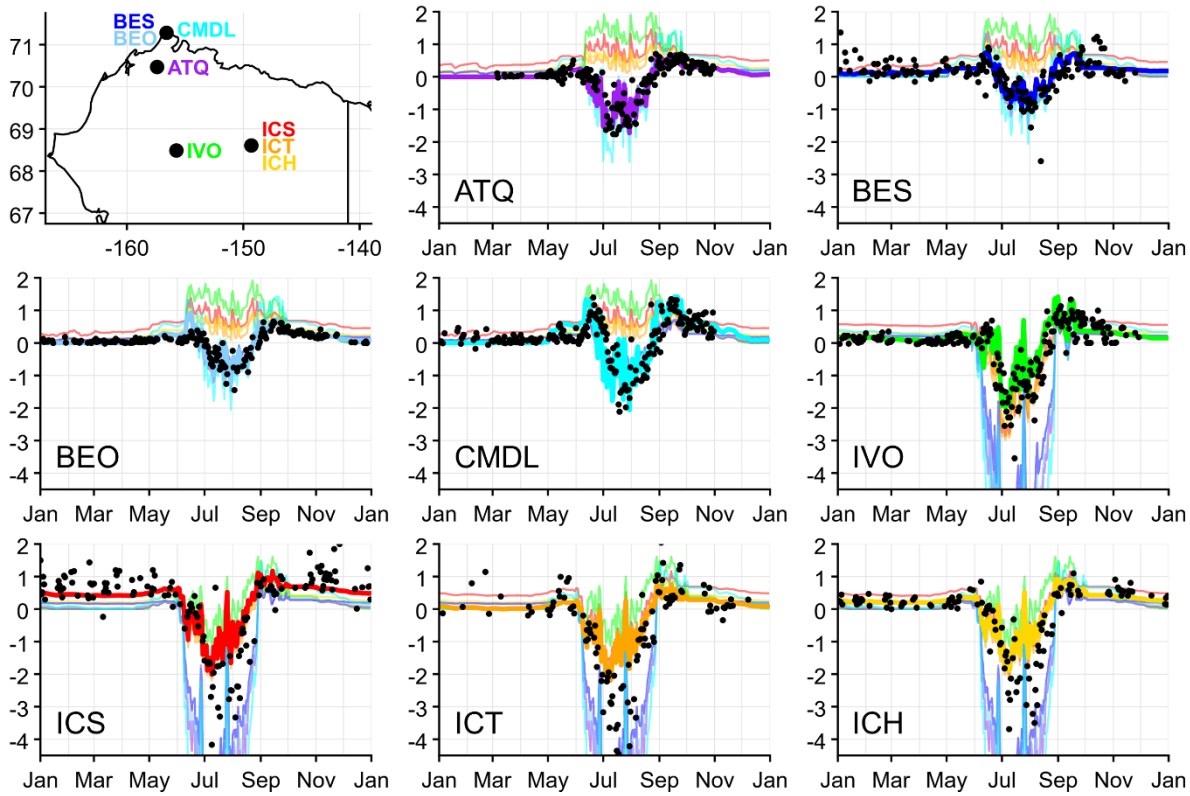
78 **S5 Scaling TVPRM from site-level to regional net CO₂ flux**

79 To scale from site-level to regional net CO₂ flux, we first calculate the hourly TVPRM net CO₂ flux at each meteorological
80 gridbox for each median variable parameter set from the eight eddy flux sites. The regional simulated net CO₂ flux at each
81 gridbox is then determined by weighting the site-specific net CO₂ flux by the fraction of each vegetation type within that
82 gridbox based on the classifications of inland tundra, coastal tundra, other land, inland water, and ocean. For each regional
83 simulation, we assume all inland tundra is represented by the parameterization from one of four sites (ICS, ICH, ICT, IVO)
84 and all coastal tundra is represented by one of the remaining sites (ATQ, BES, BEO, CMDL). This method allows for
85 separation and testing of distinct site-level responses within each group. Figure S1 shows the distinct response of TVPRM
86 using variable parameters from these two groups. Net CO₂ fluxes from other land, inland water, and ocean areas are set to 0.

87 The vegetation maps used to determine the fraction of each classification are described in Table S5. We group CAVM
88 and RasterCAVM classifications for graminoid and shrub tundra into our inland tundra classification, with wetland tundra
89 classifications used as coastal tundra. Barren, glacier, and ice/snow classifications are set to other land, and water classifications
90 remain separate for inland water and ocean. ABoVE LC classifications are grouped into our classification scheme by vegetation
91 description and spatial distribution. CAVM and RasterCAVM are proportionally scaled to match ABoVE LC for other land,

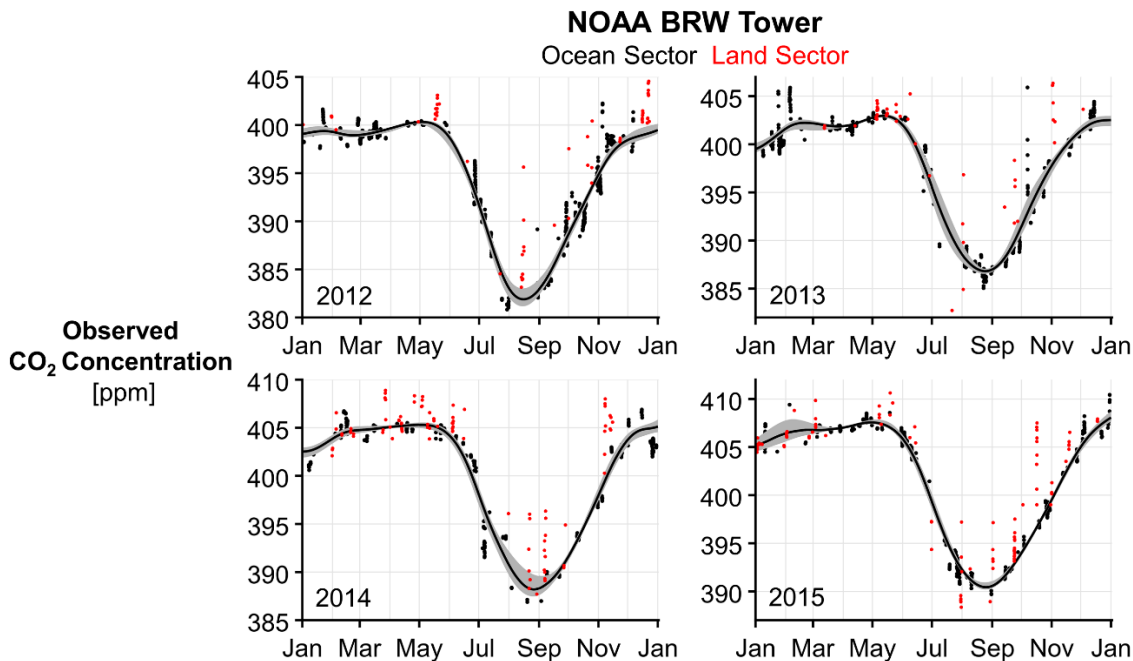
92 inland water, and ocean, so inland and coastal tundra are the only variations between the vegetation maps. Figure S5 shows
93 the distribution and percentage of these grouped classifications within our North Slope domain.

94 Spatial distribution maps throughout this study are produced by rasterizing native NARR and ERA5 gridboxes to 1
95 km boxes on the NASA Arctic-Boreal Vulnerability Experiment (ABOVE) standard projection and grid
96 (https://above.nasa.gov/implementation_plan/standard_projection.html) and aggregating these boxes to 30 km, consistent with
97 the native spatial resolution. Regional flux values are calculated using gridbox fluxes on native resolution.

Daily Mean Site-level Net CO₂ Flux [$\mu\text{mol m}^{-2} \text{s}^{-1}$]

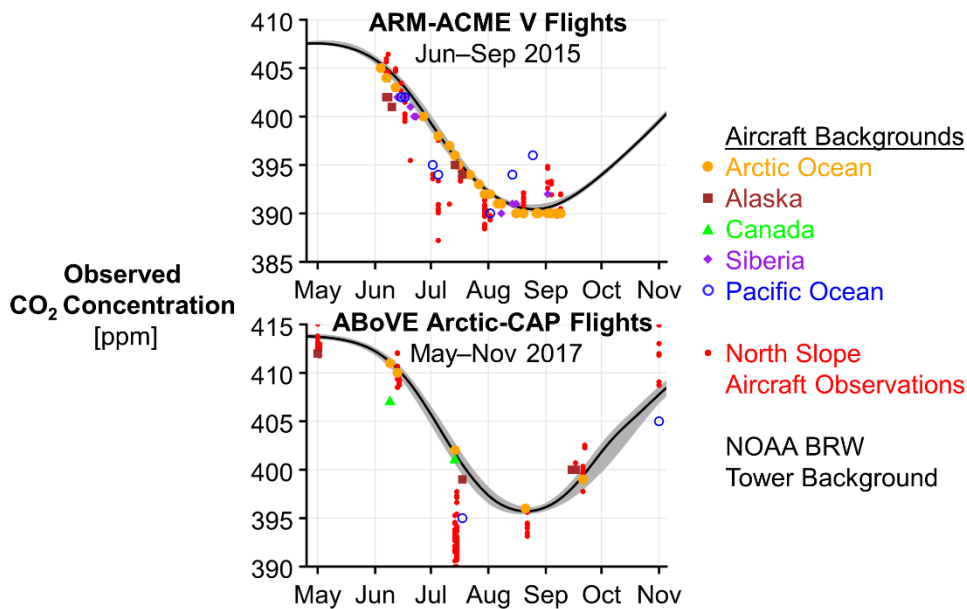
99

100 **Figure S1.** Timeseries of daily mean site-level net CO₂ flux for 2014 at eddy flux measurement sites used to determine TVPRM parameters.
 101 Colored lines shows TVPRM simulated net CO₂ flux using parameters for each of the eight sites that is driven by NARR meteorology and
 102 CSIF SIF product at each site location (individual panes). Lines for matching site parameters and locations are highlighted. Black dots show
 103 observed net CO₂ flux at each site. Locations of eddy flux measurement sites on the Alaska North Slope shown in upper left.



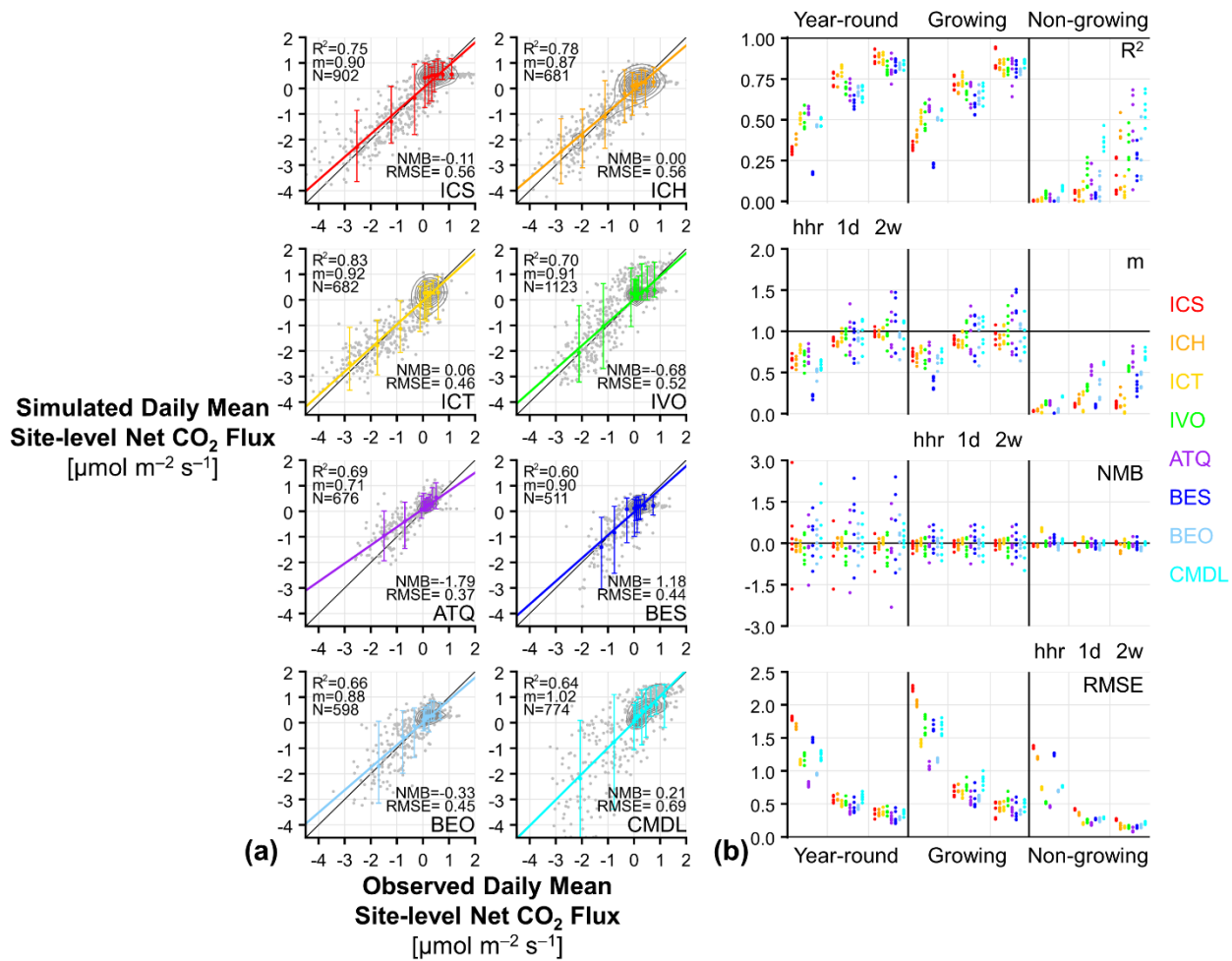
104

105 **Figure S2.** Timeseries of calculated NOAA BRW tower ocean sector CO₂ background concentration (black line) for 2012–2015. Uncertainty
 106 (95% of results) determined by varying start time of spline fit and repeatedly randomly removing 50% of used points shown by gray ribbon.
 107 Black dots indicate ocean sector hourly observations used in spline fit, and red dots indicate land sector hourly observations used in model
 108 evaluation (Figs. 2c–2d, 3b–3c, 4a, 4c, S11, S14).



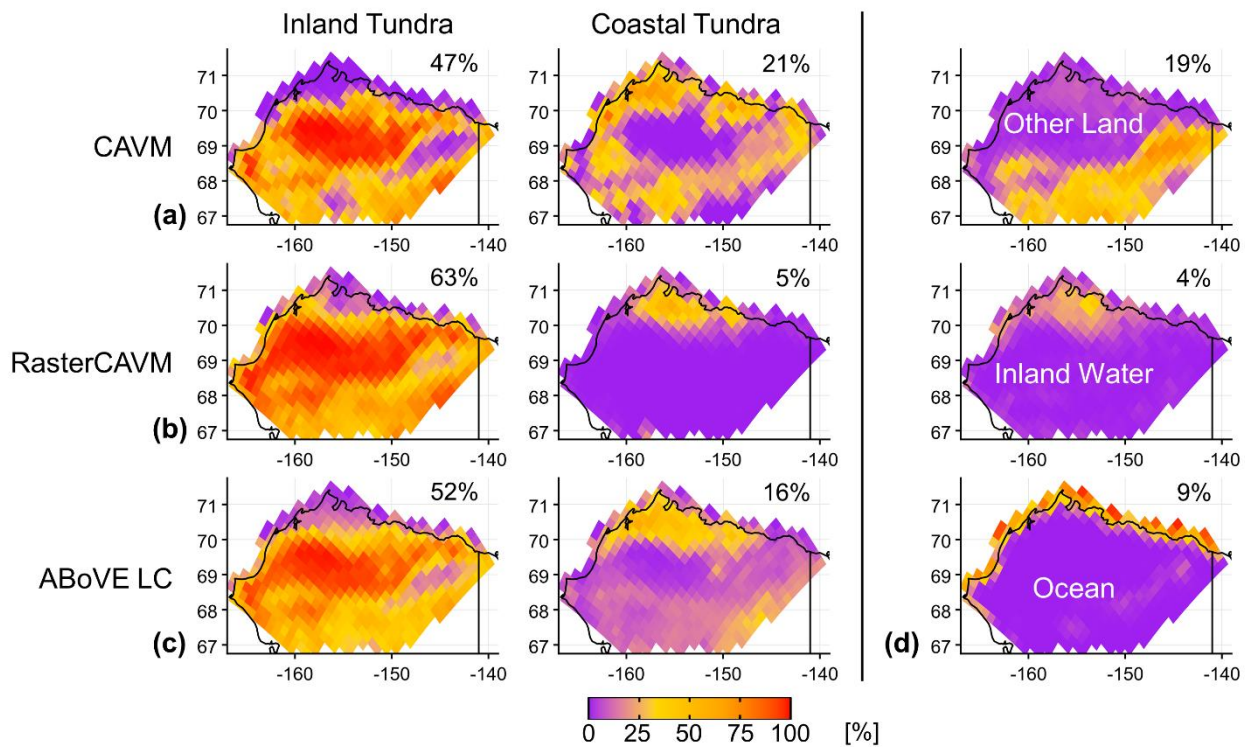
109

110 **Figure S3.** Timeseries of CO₂ background concentration determined using aircraft observations without Alaska North Slope surface
 111 influence for the ARM-ACME V and ABoVE Arctic-CAP flight campaigns. Various colored symbols indicate the background source region.
 112 Red dots show aircraft observations used in model evaluation (Figs. 2a–2b, 2d, S8). NOAA BRW tower ocean sector background (median
 113 and uncertainty) also shown as in Fig. S2.



114

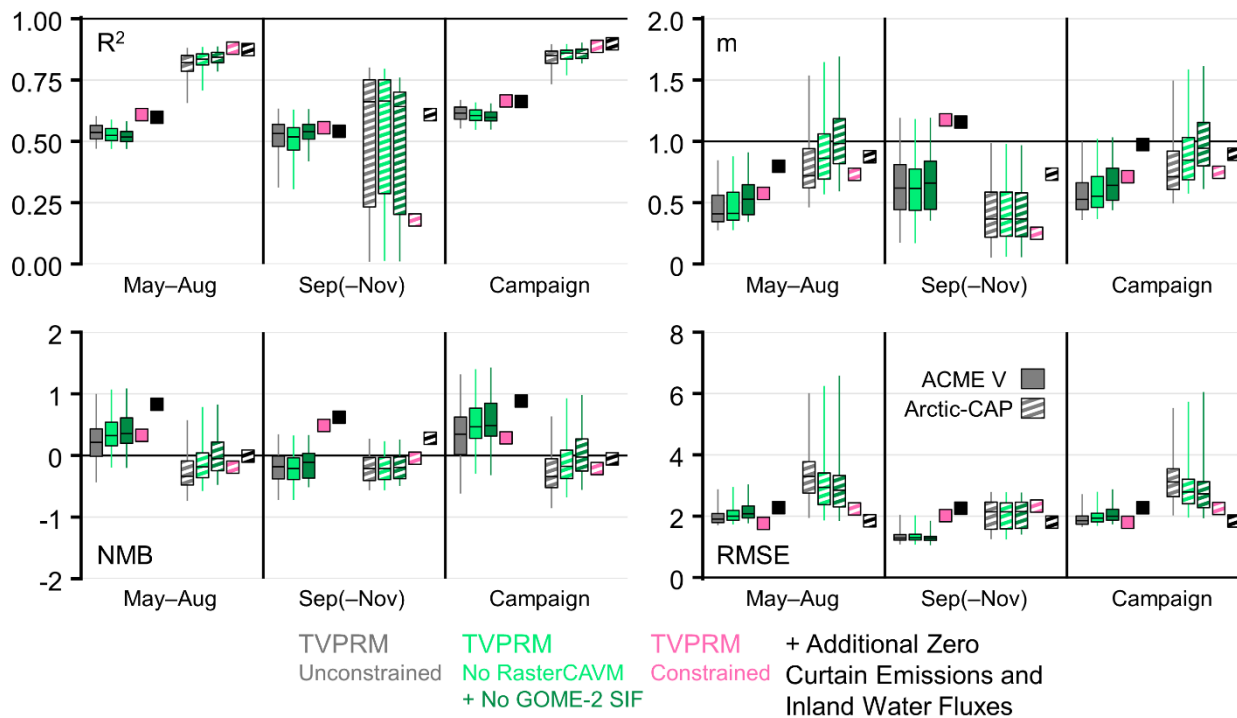
115 **Figure S4.** (a) Comparison of observed and simulated TPVRM daily mean site-level net CO₂ flux (gray dots) for 2013–2017 at eddy flux
 116 measurement sites used to determine TVPRM parameters, where TVPRM is driven by ERA5 meteorology and the CSIF SIF product. In
 117 each comparison, contours contain 10% of all points, and vertical bars indicate 95% distribution and colored dots indicate median of
 118 simulated values within each 10% bin of observations. Statistics shown for each comparison include coefficient of determination of all points
 119 (R^2), slope (m) determined by ordinary least squares using median of each 10% bin of observations, number of points (N), normalized mean
 120 bias (NMB) of all points, and root-mean-square error (RMSE) of all points. 1:1 line shown in dark gray. (b) Comparison statistics as in (a)
 121 for various TVPRM environmental drivers (six combinations of NARR and ERA5 meteorology with GOME-2, GOSIF, and CSIF SIF) over
 122 various averaging lengths (half-hour (hr), one day (1d), two weeks (2w)) for various timeframes (year-round, growing season, non-growing
 123 season). Optimal value for each statistic shown as horizontal black line.



124

125 **Figure S5.** Spatial distribution of (a)–(c) inland and coastal tundra classification for (a) CAVM, (b) RasterCAVM, and (c) ABoVE LC
 126 vegetation maps and (d) other land, inland water, and ocean classifications for ABoVE LC vegetation map. Percentage of Alaska North
 127 Slope domain represented by each classification in upper right.

Observed v. Simulated ΔCO_2 ARM-ACME V 2015 and ABoVE Arctic-CAP 2017 Flights

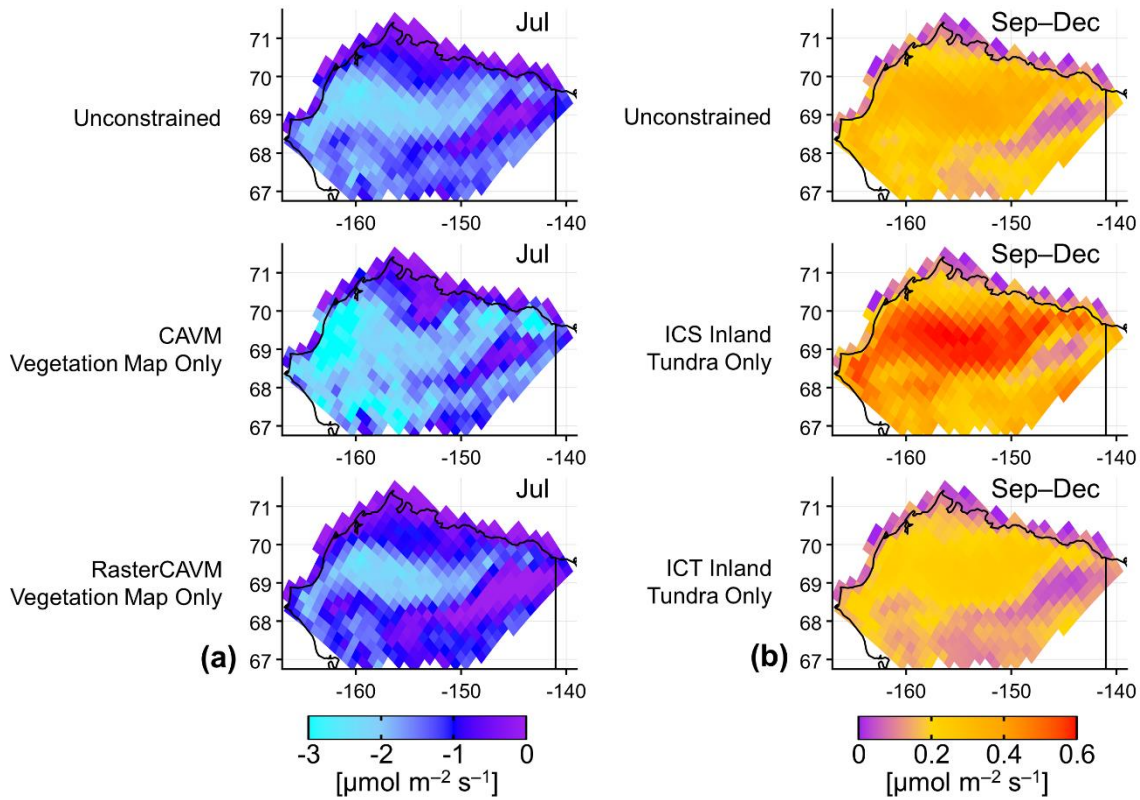


128

129 **Figure S6.** Statistics for comparison of observed and simulated ΔCO_2 during the ARM-ACME V and (solid fill) ABoVE Arctic-CAP (striped
 130 fill) aircraft campaign for various segments of the TVPRM ensemble (see legend) for various timeframes (growing season (May–Aug), early
 131 cold season (Sep(–Nov), ABoVE Arctic-CAP only)), entire campaign). Each comparison includes the coefficient of determination of all
 132 points (R^2), slope (m) determined by ordinary least squares using median of each 10% bin of observations, normalized mean bias (NMB) of
 133 all points, and root-mean-square error (RMSE) of all points. Optimal value for each statistic shown as horizontal black line.

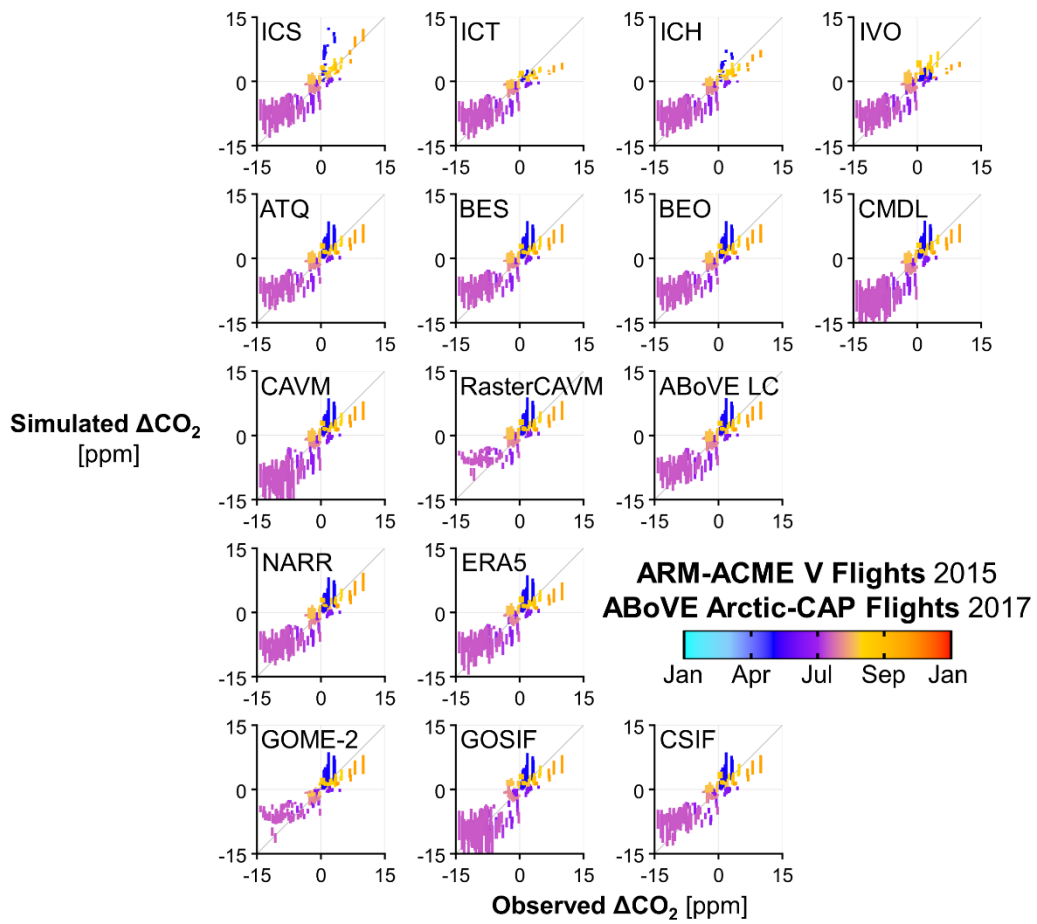
Median TVPRM Net CO₂ Flux
2015, 2017

Median TVPRM Net CO₂ Flux
2012–2015



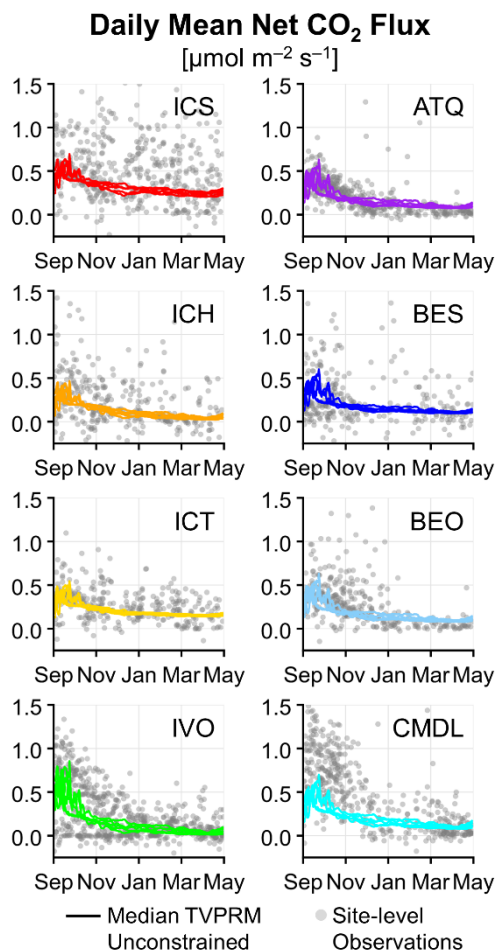
134

135 **Figure S7.** (a) Spatial distribution of mean July TVPRM net CO₂ flux for 2015 and 2017. Median value is shown for multiple TPVRM
 136 members using all vegetation maps (top), only CAVM vegetation map (middle), and only RasterCAVM vegetation map (bottom). Colors
 137 are saturated at $-3 \mu\text{mol m}^{-2} \text{s}^{-1}$. (b) Spatial distribution of mean Sep–Dec TVPRM net CO₂ flux for 2012–2015. Median value is shown for
 138 multiple TVPRM members using all inland site parameterizations (top), only ICS inland site parameterization (middle), and only ICT inland
 139 site parameterization (bottom). Colors are saturated at $0.6 \mu\text{mol m}^{-2} \text{s}^{-1}$.



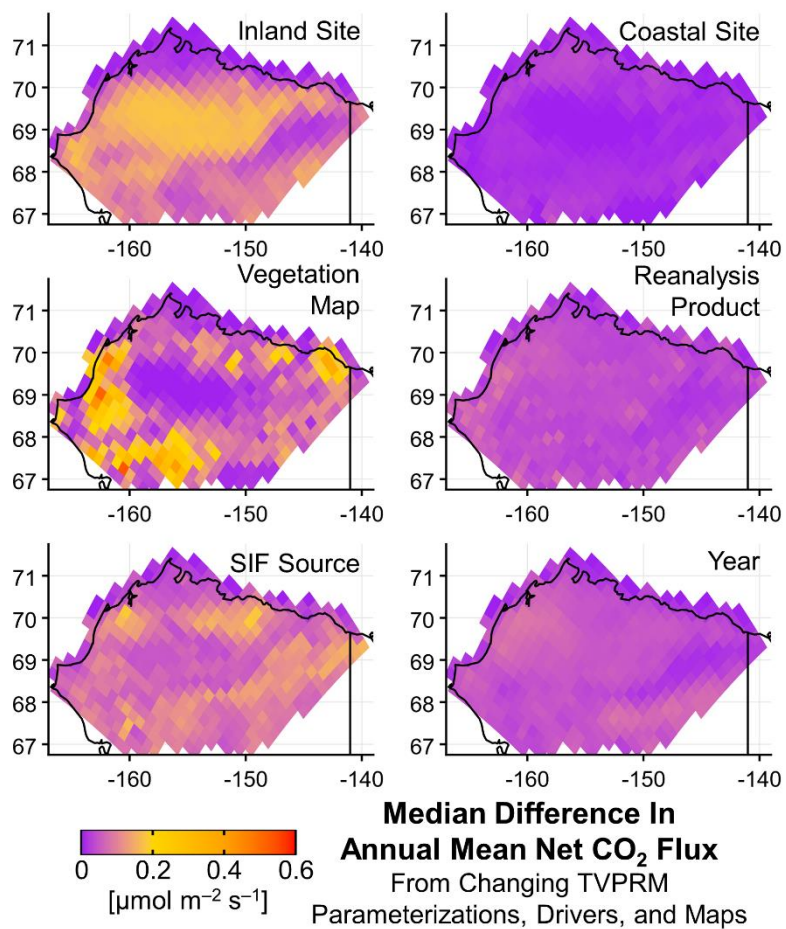
140

141 **Figure S8.** Comparison of vertically binned median observed and TVPRM simulated ΔCO_2 during the ARM-ACME V and ABoVE Arctic-
 142 CAP flight campaigns over the Alaska North Slope isolated for each model parameterization or driver. Vertical boxes represent 50% of
 143 ΔCO_2 values from remaining TVPRM members from all binned points. 1:1 line shown in dark gray.



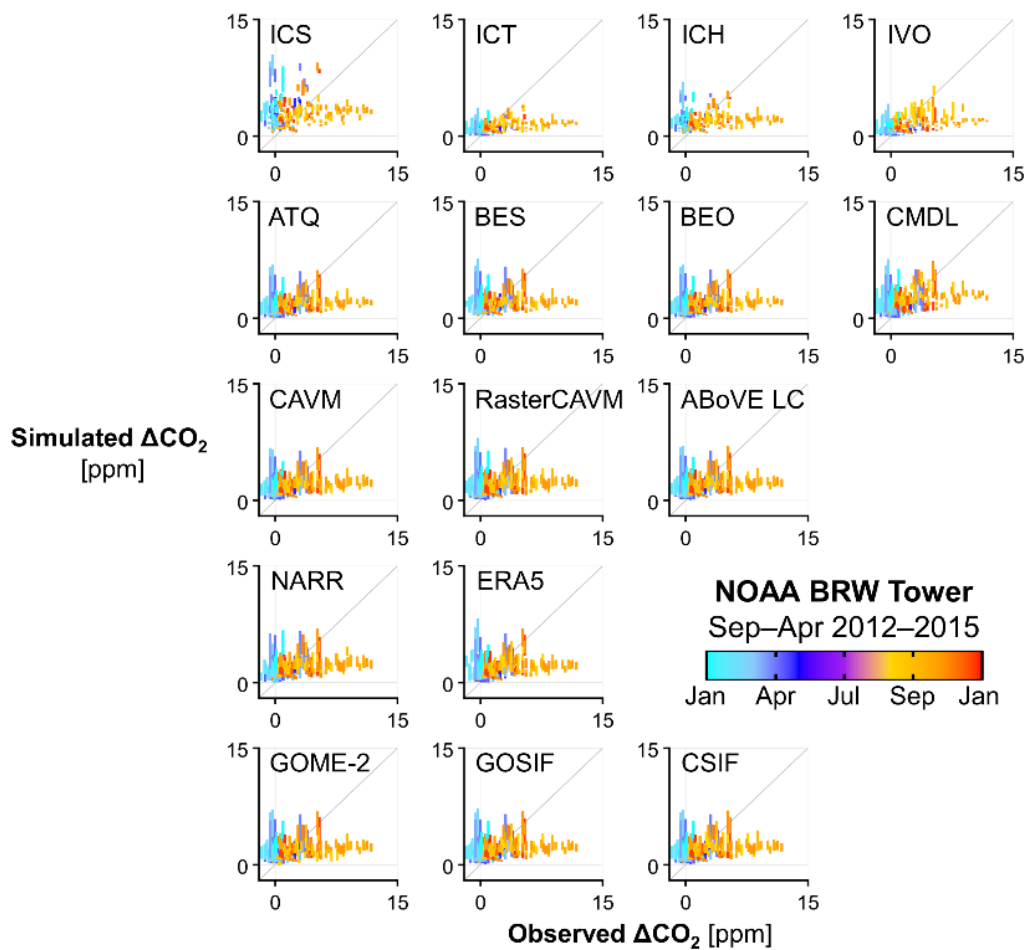
144

145 **Figure S9.** Observed daily mean site-level (grey points) and simulated daily mean Alaska North Slope (colored lines) net CO₂ flux at eight
 146 eddy flux sites for cold seasons (Sep–Apr) of 2012–2017. Simulated net CO₂ flux is for the median of all unconstrained TVPRM ensemble
 147 members using the observation-derived parameterizations from that eddy flux site.



148

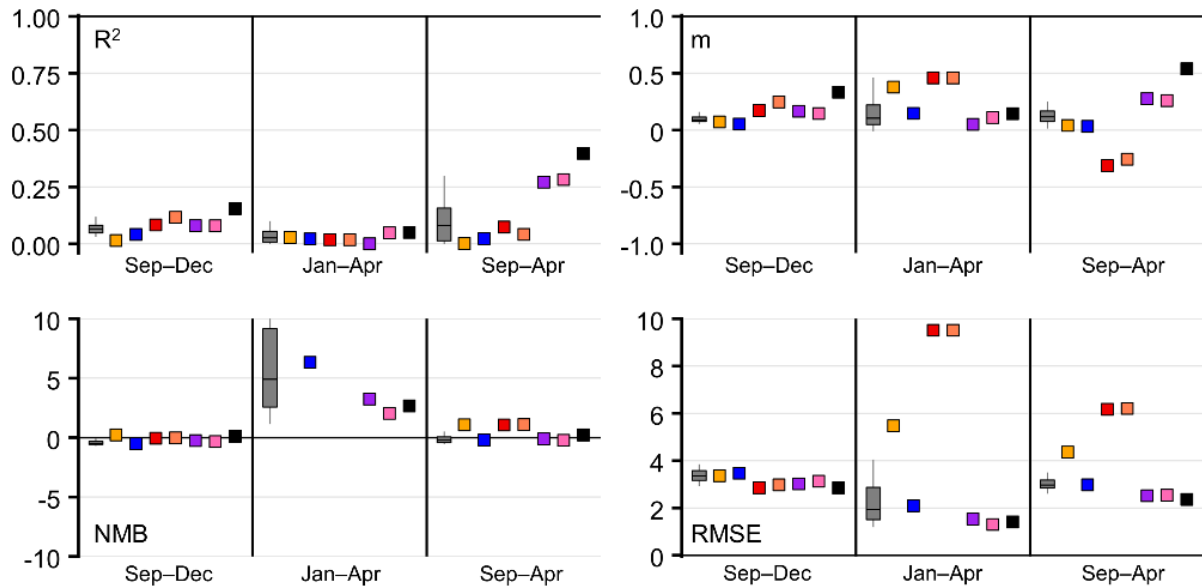
149 **Figure S10.** Spatial distribution of median difference in annual mean net CO₂ flux change driven by changing unconstrained TVPRM
 150 ensemble site-level parameterizations, environmental drivers, and vegetation distributions for 2012–2017 on the Alaska North Slope. Colors
 151 are saturated at 0.6 $\mu\text{mol m}^{-2} \text{s}^{-1}$.



152

153 **Figure S11.** Comparison of hourly cold season (Sep–Apr) observed and TVPRM simulated ΔCO_2 at the NOAA BRW tower isolated for
 154 each model parameterization or driver. Vertical boxes represent 50% of ΔCO_2 values from remaining TVPRM members. 1:1 line shown in
 155 dark gray.

**Observed v. Simulated ΔCO_2
NOAA BRW Tower 2012–2015**



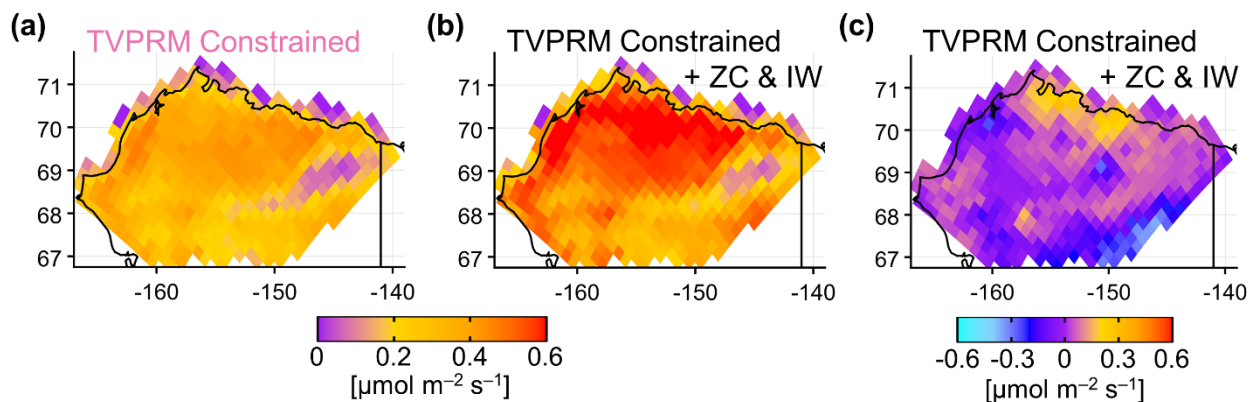
TVPRM Unconstrained Natali & Watts et al. (2019) Luus et al. (2017) TVPRM TVPRM + Additional Zero
Watts et al. (2021) Commane et al. (2017) Constrained Constrained Curtain Emissions and
RS-PM T_{soil} Inland Water Fluxes

156

157 **Figure S12.** Statistics for comparison of observed and simulated ΔCO_2 at the NOAA BRW tower for various CO_2 flux models (see legend)
 158 for various timeframes (early cold season (Sep–Dec), late cold season (Jan–Apr), entire cold season (Sep–Apr)). Each comparison includes
 159 the coefficient of determination of all points (R^2), slope (m) determined by ordinary least squares using median of each 10% bin of
 160 observations, normalized mean bias (NMB) of all points, and root-mean-square error (RMSE) of all points. Optimal value for each statistic
 161 shown as horizontal black line.

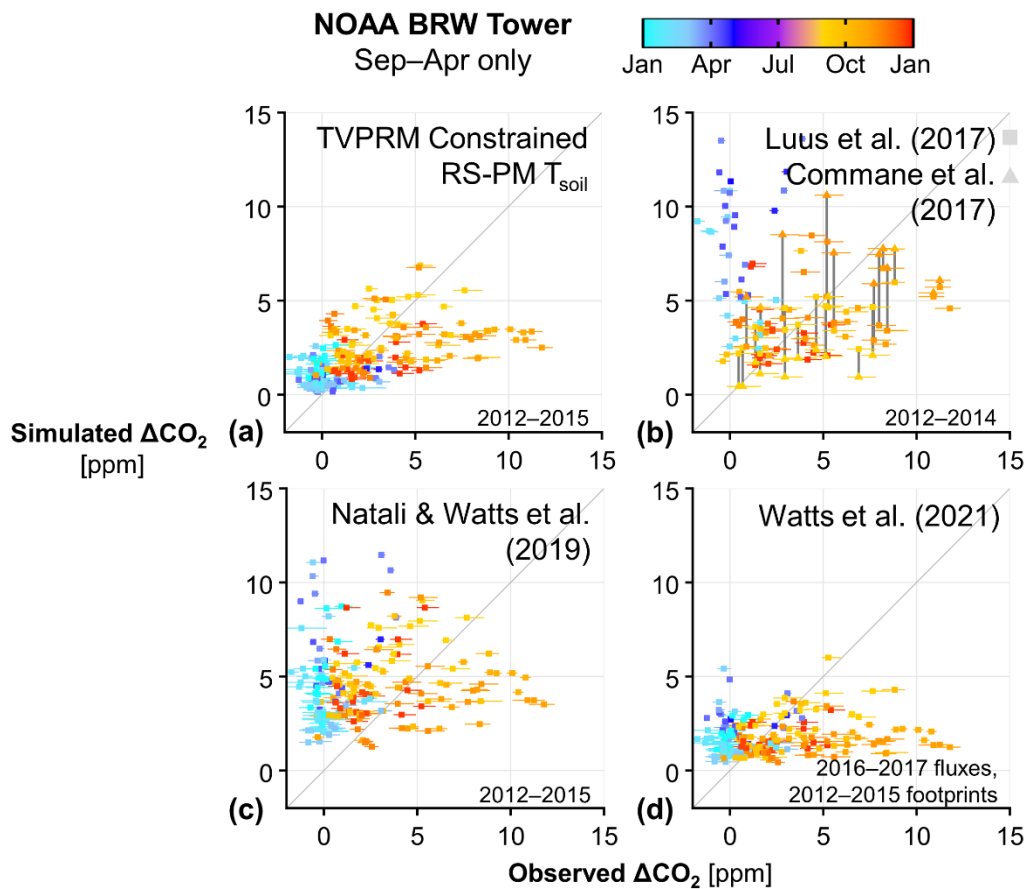
Sep–Dec Mean Net CO₂ Flux
2012–2015

Annual Mean Net CO₂ Flux
2012–2015



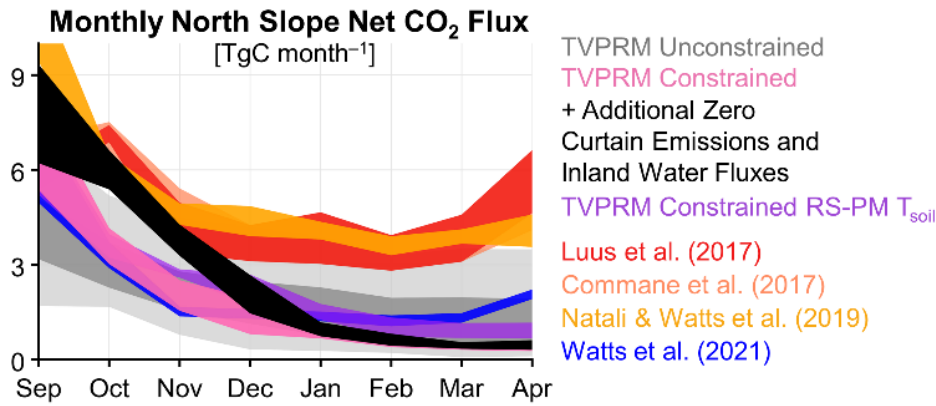
162

163 **Figure S13.** (a)–(b) Spatial distribution of early cold season (Sep–Dec) mean TVPRM net CO₂ flux for 2012–2015 for constrained TVPRM
164 member + additional zero-curtain emissions (ZC) and inland water fluxes (IW). Colors are saturated at 0.6 $\mu\text{mol m}^{-2} \text{s}^{-1}$. (c) Spatial
165 distribution of annual mean constrained TVPRM member + ZC & IW net CO₂ flux for 2012–2015. Colors are saturated at $\pm 0.6 \mu\text{mol m}^{-2}$
166 s^{-1} .



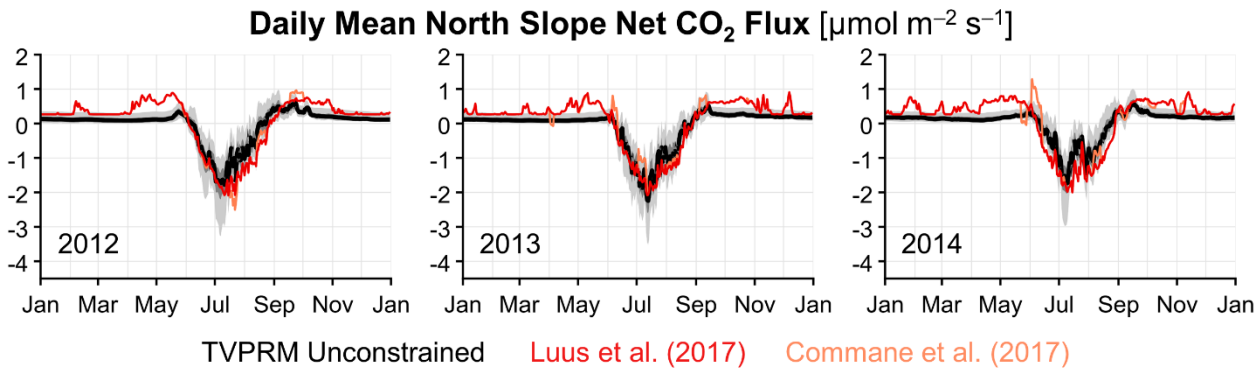
167

168 **Figure S14.** Comparison of hourly cold season (Sep–Apr) observed and simulated ΔCO_2 at the NOAA BRW tower using various CO_2 flux
 169 models and timeframes. Horizontal segments indicate range of uncertainty in the BRW tower ocean sector background calculation. For (b),
 170 vertical gray bars connect corresponding points in the net CO_2 flux model values from Luus et al. (2017) and Commane et al. (2017). 1:1
 171 line shown in dark gray.



172

173 **Figure S15.** Monthly cold season total Alaska North Slope CO₂ fluxes for various CO₂ flux models shown in Figs. 4 and S14. The net CO₂
 174 fluxes from the TVPRM ensemble and members and from Natali & Watts et al. (2019) show values for 2012–2017, from Luus et al. (2017)
 175 and Commane et al. (2017) show 2012–2014, and from Watts et al. (2021) show Sep 2016–Apr 2017. Ribbons represent range of all years,
 176 where applicable, except for unconstrained TVPRM ensemble, where dark gray ribbon represents 50% and light gray ribbon represents 95%
 177 of CO₂ flux values from all members for 2012–2017. Area of North Slope domain used to calculate regional totals is 3.537×10^5 km².

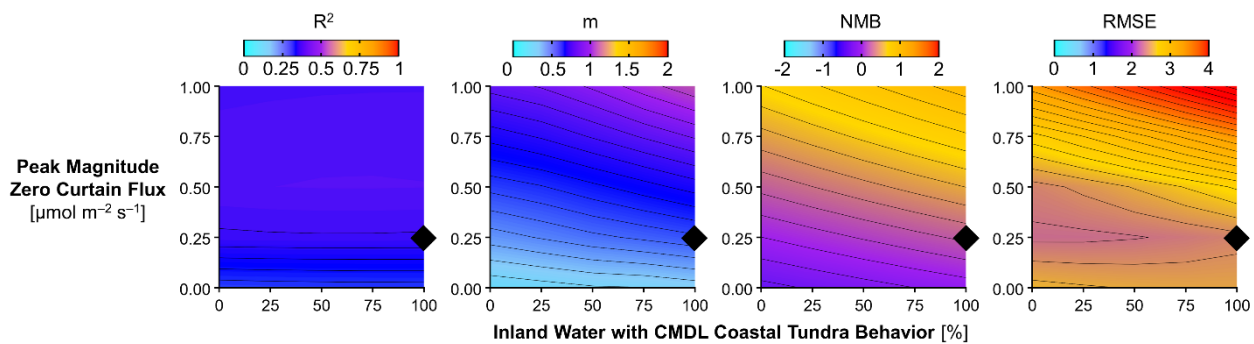


178

179 **Figure S16.** Timeseries of simulated daily mean Alaska North Slope net CO₂ flux for 2012–2014. Black line indicates median, dark gray
 180 ribbon represents 50%, and light gray ribbon represents 95% of daily mean net CO₂ flux values from all members of unconstrained TVPRM
 181 ensemble. Light red and dark red lines indicate daily mean net CO₂ flux values from Luus et al. (2017) and Commane et al. (2017),
 182 respectively.

Observed v. Simulated ΔCO_2
NOAA BRW Tower Sep–Apr 2012–2015

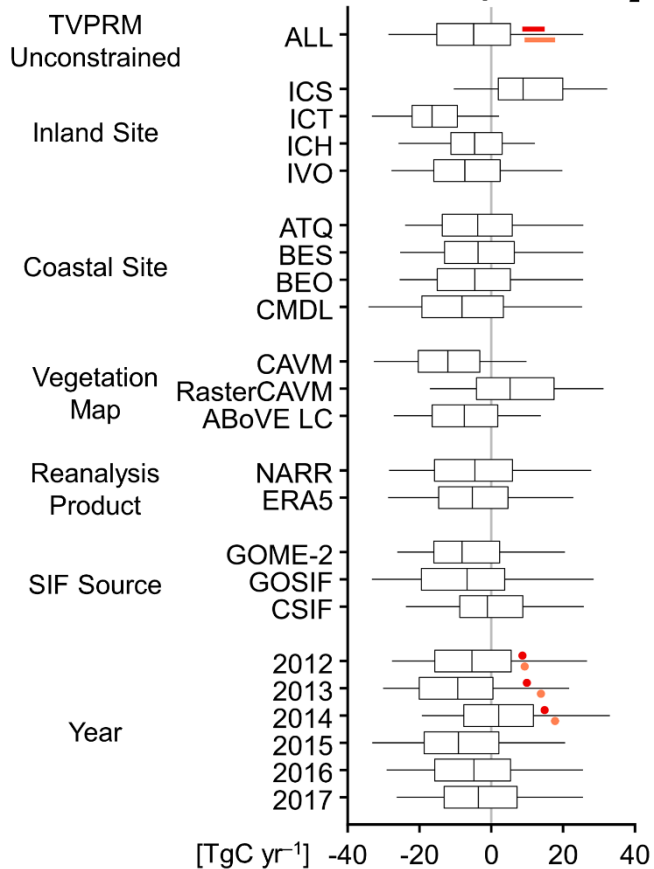
TVPRM Constrained + Additional Zero
Curtain Emissions and Inland Water Fluxes



183

184 **Figure S17.** Statistics for comparison of observed and simulated ΔCO_2 at the NOAA BRW tower for the cold season (Sep–Apr) as calculated
185 in Fig. S12. Simulated ΔCO_2 is determined using the constrained TVPRM member with varying amounts of inland water (IW) area
186 represented as CMDL coastal tundra site parameterization (horizontal axis) and additional peak zero curtain (ZC) flux (vertical axis). Black
187 diamonds indicate best performing combination and choice for ZC+IW formulation. Colors are saturated at shown colorbar endpoints.

Annual North Slope Net CO₂ Flux



188

189 **Figure S18.** Range of annual North Slope net CO₂ flux from the TVPRM ensemble determined by various ecological parameterizations,
 190 environmental drivers, and vegetation distributions for 2012–2017 (black) and from the net CO₂ flux models by Luus et al. (2017) (dark red)
 191 and Commane et al. (2017) (light red) for 2012–2014. For each site parameterization or driver, boxes represent 50% and whiskers represent
 192 95% of the net CO₂ flux from all TVPRM members included in that category. Area of North Slope domain used to calculate regional totals
 193 is 3.537×10^5 km².

194 **Supplemental Tables**

195 **Table S1.** Alaska North Slope eddy covariance flux sites measuring net CO₂ flux for 2013–2017 used in this study. See Figs. 1c and S1 for
 196 map of site locations. ATQ, BES, BEO, CMDL, and IVO are further described by Zona et al. (2016) and Arndt et al. (2020). ICS, ICT, and
 197 ICH are further described by Euskirchen et al. (2012) and Euskirchen et al. (2017).

Site ID	Name	Ecosystem / TVPRM Group	Vegetation	Data Coverage (month/year)
ATQ	Atqasuk	Wet polygonised tundra / coastal	Water sedge, dwarf shrub	09/2013–11/2013, 02/2014–10/2014, 02/2015–01/2016, 07/2016, 09/2016–04/2017, 06/2017–07/2017, 09/2017–12/2017
BES	Barrow Biocomplexity Experiment, South	Wetland tundra / coastal	Sedge, moss	07/2013–11/2014, 02/2015–10/2015, 07/2016–01/2017, 05/2017–07/2017
BEO	Barrow Environmental Observatory	Wet polygonised tundra / coastal	Graminoid grass, sedge	09/2013–01/2015, 06/2015–02/2016, 04/2016–07/2016, 07/2017–12/2017
CMDL	Barrow Climate Monitoring and Diagnostics Laboratory	Moist tundra / coastal	Graminoid grass, lichen	10/2013–10/2014, 02/2015–05/2015, 07/2015–09/2017, 11/2017–12/2017
IVO	Ivotuk	Tussock tundra / inland	Tussock-forming sedge, moss	06/2013–11/2014, 02/2015–12/2017
ICS	Imnavait Creek Wet Sedge	Wet sedge tundra / inland	Water sedge, swarf deciduous shrub, moss	01/2013–12/2017
ICH	Imnavait Creek Heath Tundra	Dry heath tundra / inland	Dwarf evergreen shrub, deciduous shrub, lichen	01/2013–12/2016, 03/2017–12/2017
ICT	Imnavait Creek Tussock Tundra	Moist acidic tussock tundra / inland	Tussock-forming sedge, deciduous dwarf shrub, evergreen dwarf shrub	01/2013–12/2014, 04/2015–12/2017

198

199 **Table S2.** Previously developed CO₂ flux models used in this study.

Model ID	Model Resolution / Years	Model Details
Luus et al. (2017)	1/4° × 1/6° spatial, 3 hourly temporal / 2012–2014	Similar to TPVRM, using monthly SIF values and alternative eddy flux sites and methods to calculate variable parameters. Accounts for both boreal and tundra ecosystems.
Commane et al. (2017)	0.5° spatial, 3 hourly temporal / 2012–2014	Luus et al. (2017) optimized based on observations from the Carbon in Arctic Reservoirs Vulnerability Experiment (CARVE) flight campaign. Reverts to Luus et al. (2017) for time periods without flights.
Natali & Watts et al. (2019)	25 km spatial, monthly temporal / 2012–2015	Synthesis of pan-Arctic winter in situ CO ₂ flux observations and environmental drivers using boosted regression tree machine learning.
Watts et al. (2021)	300 m spatial, monthly temporal / 2016–2017	Integration of Alaskan and northwest Canadian belowground CO ₂ flux observations and satellite data using random forest machine learning.

200

201 **Table S3.** Reanalysis meteorology products for 2012-2017 used by TVPRM in this study.

Met ID	Product Name	Product Resolution	Product Variable used in TVPRM		
			T _a	T _s	PAR
NARR	NOAA North American Regional Reanalysis Mesinger et al. (2006)	~30 km spatial, 3 hourly temporal	air.2m	tsoil (10 cm)	dswrf
ERA5	ECMWF Reanalysis, fifth generation Hersbach et al. (2020)	~31 km spatial, hourly temporal	t2m	stl2 (7–28 cm)	ssrd

202

203 **Table S4.** SIF products for 2012-2017 used by TVPRM in this study.

SIF ID	Product Name	Product Resolution	Product Details
GOME-2	Interpolated GOME-2 SIF (created for this study) [GOME-2: Global Ozone Monitoring Experiment-2]	0.01° latitudinal, daily temporal	Discrete GOME-2 SIF v27 retrievals (Joiner et al., 2016), normalized by solar zenith angle, averaged by center point into overlapping 0.5° latitudinal bins across the North Slope domain. Temporal interpolation within each bin and latitudinal interpolation across bins applied using loess fit smoothing.
GOSIF	Global ‘OCO-2’ SIF (Li and Xiao, 2019) [OCO-2: Orbiting Carbon Observatory-2]	0.05° spatial, 8 day temporal	Aggregated OCO-2 soundings combined with MODIS enhanced vegetation index and MERRA-2 PAR, vapor pressure deficit, and air temperature to create a higher resolution gridded SIF product using multivariate linear regression.
CSIF	Contiguous SIF (Zhang et al., 2018)	0.05° spatial, 4 day temporal	Aggregated OCO-2 soundings combined with MODIS surface reflectance to create a higher resolution gridded SIF product using a neural network.

204 **Table S5.** Vegetation maps used by TVPRM in this study.

Map ID	Map Name	Map Resolution / Year	Map Classification Details
CAVM	Circumpolar Arctic Vegetation Map (Walker et al., 2005)	14 km polygons, 8 km linear features / satellite data from 1993 and 1995, developed in 2003	15 classification units based on plant growth forms, roughly separated by summer temperature and soil moisture. Polygon classification from combination of satellite, vegetation, temperature, topographic, and geologic data.
RasterCAVM	Raster version of CAVM (Raynolds et al., 2019)	1 km spatial / satellite data as in CAVM, additional data from 2000–2009	Classification as in CAVM, redistributed at higher resolution based on unsupervised classification using satellite and elevation data.
ABoVELC	Landsat-derived Annual Dominant Land Cover across ABoVE Core Domain (Wang et al., 2020)	30 m spatial / 2014 [ABoVE: Arctic-Boreal Vulnerability Experiment]	15 classification units based on semi-supervised classification using satellite, climate, and topographic data

205

206 Supplemental References

207 Arndt, K. A., Lipson, D. A., Hashemi, J., Oechel, W. C., and Zona, D.: Snow melt stimulates ecosystem respiration in Arctic
208 ecosystems, *Global Change Biol.*, 26, 5042–5051, <https://doi.org/10.1111/gcb.15193>, 2020.

209 Commane, R., Lindaas, J., Benmergui, J., Luus, K. A., Chang, R. Y.-W., Daube, B. C., Euskirchen, E. S., Henderson, J. M.,
210 Karion, A., Miller, J. B., Miller, S. M., Parazoo, N. C., Randerson, J. T., Sweeney, C., Tans, P., Thoning, K., Veraverbeke, S.,
211 Miller, C. E., and Wofsy, S. C.: Carbon dioxide sources from Alaska driven by increasing early winter respiration from Arctic
212 tundra, *PNAS*, 114, 5361–5366, <https://doi.org/10.1073/pnas.1618567114>, 2017.

213 Euskirchen, E. S., Bret-Harte, M. S., Scott, G. J., Edgar, C., and Shaver, G. R.: Seasonal patterns of carbon dioxide and water
214 fluxes in three representative tundra ecosystems in northern Alaska, *Ecosphere*, 3, art4, <https://doi.org/10.1890/ES11-00202.1>,
215 2012.

216 Euskirchen, E. S., Bret-Harte, M. S., Shaver, G. R., Edgar, C. W., and Romanovsky, V. E.: Long-Term Release of Carbon
217 Dioxide from Arctic Tundra Ecosystems in Alaska, *Ecosystems*, 20, 960–974, <https://doi.org/10.1007/s10021-016-0085-9>,
218 2017.

219 Hersbach, H., Bell, B., Berrisford, P., Hirahara, S., Horányi, A., Muñoz-Sabater, J., Nicolas, J., Peubey, C., Radu, R., Schepers,
220 D., Simmons, A., Soci, C., Abdalla, S., Abellan, X., Balsamo, G., Bechtold, P., Biavati, G., Bidlot, J., Bonavita, M., Chiara,
221 G. D., Dahlgren, P., Dee, D., Diamantakis, M., Dragani, R., Flemming, J., Forbes, R., Fuentes, M., Geer, A., Haimberger, L.,
222 Healy, S., Hogan, R. J., Hólm, E., Janisková, M., Keeley, S., Laloyaux, P., Lopez, P., Lupu, C., Radnoti, G., Rosnay, P. de,
223 Rozum, I., Vamborg, F., Villaume, S., and Thépaut, J.-N.: The ERA5 global reanalysis, *Q. J. Roy. Meteorol. Soc.*, 146, 1999–
224 2049, <https://doi.org/10.1002/qj.3803>, 2020.

- 225 Joiner, J., Yoshida, Y., Guanter, L., and Middleton, E. M.: New methods for the retrieval of chlorophyll red fluorescence from
 226 hyperspectral satellite instruments: simulations and application to GOME-2 and SCIAMACHY, *Atmos. Meas. Tech.*, 9, 3939–
 227 3967, <https://doi.org/10.5194/amt-9-3939-2016>, 2016.
- 228 Li, X. and Xiao, J.: A Global, 0.05-Degree Product of Solar-Induced Chlorophyll Fluorescence Derived from OCO-2, MODIS,
 229 and Reanalysis Data, *Remote Sens.*, 11, 517, <https://doi.org/10.3390/rs11050517>, 2019.
- 230 Luus, K. A., Commane, R., Parazoo, N. C., Benmergui, J., Euskirchen, E. S., Frankenberg, C., Joiner, J., Lindaas, J., Miller,
 231 C. E., Oechel, W. C., Zona, D., Wofsy, S., and Lin, J. C.: Tundra photosynthesis captured by satellite-observed solar-induced
 232 chlorophyll fluorescence, *Geophys. Res. Lett.*, 44, 2016GL070842, <https://doi.org/10.1002/2016GL070842>, 2017.
- 233 Mesinger, F., DiMego, G., Kalnay, E., Mitchell, K., Shafran, P. C., Ebisuzaki, W., Jović, D., Woollen, J., Rogers, E., Berbery,
 234 E. H., Ek, M. B., Fan, Y., Grumbine, R., Higgins, W., Li, H., Lin, Y., Manikin, G., Parrish, D., and Shi, W.: North American
 235 Regional Reanalysis, *B. Am. Meteorol. Soc.*, 87, 343–360, <https://doi.org/10.1175/BAMS-87-3-343>, 2006.
- 236 Natali, S. M., Watts, J. D., Rogers, B. M., Potter, S., Ludwig, S. M., Selbmann, A.-K., Sullivan, P. F., Abbott, B. W., Arndt,
 237 K. A., Birch, L., Björkman, M. P., Bloom, A. A., Celis, G., Christensen, T. R., Christiansen, C. T., Commane, R., Cooper, E.
 238 J., Crill, P., Czimczik, C., Davydov, S., Du, J., Egan, J. E., Elberling, B., Euskirchen, E. S., Friborg, T., Genet, H., Göckede,
 239 M., Goodrich, J. P., Grogan, P., Helbig, M., Jafarov, E. E., Jastrow, J. D., Kalhori, A. A. M., Kim, Y., Kimball, J. S., Kutzbach,
 240 L., Lara, M. J., Larsen, K. S., Lee, B.-Y., Liu, Z., Lorant, M. M., Lund, M., Lupascu, M., Madani, N., Malhotra, A., Matamala,
 241 R., McFarland, J., McGuire, A. D., Michelsen, A., Minions, C., Oechel, W. C., Olefeldt, D., Parmentier, F.-J. W., Pirk, N.,
 242 Poulter, B., Quinton, W., Rezanezhad, F., Risk, D., Sachs, T., Schaefer, K., Schmidt, N. M., Schuur, E. A. G., Semenchuk, P.
 243 R., Shaver, G., Sonnentag, O., Starr, G., Treat, C. C., Waldrop, M. P., Wang, Y., Welker, J., Wille, C., Xu, X., Zhang, Z.,
 244 Zhuang, Q., and Zona, D.: Large loss of CO₂ in winter observed across the northern permafrost region, *Nat. Clim. Change*,
 245 9, 852–857, <https://doi.org/10.1038/s41558-019-0592-8>, 2019.
- 246 Reynolds, M. K., Walker, D. A., Balser, A., Bay, C., Campbell, M., Cherosov, M. M., Daniëls, F. J. A., Eidesen, P. B.,
 247 Ermokhina, K. A., Frost, G. V., Jędrzejek, B., Jorgenson, M. T., Kennedy, B. E., Kholod, S. S., Lavrinenko, I. A., Lavrinenko,
 248 O. V., Magnússon, B., Matveyeva, N. V., Metúsalemsson, S., Nilsen, L., Olthof, I., Pospelov, I. N., Pospelova, E. B., Pouliot,
 249 D., Razzhivin, V., Schaepman-Strub, G., Šibík, J., Telyatnikov, M. Yu., and Troeva, E.: A raster version of the Circumpolar
 250 Arctic Vegetation Map (CAVM), *Remote Sens. Environ.*, 232, 111297, <https://doi.org/10.1016/j.rse.2019.111297>, 2019.
- 251 Walker, D. A., Reynolds, M. K., Daniëls, F. J. A., Einarsson, E., Elvebakk, A., Gould, W. A., Katenin, A. E., Kholod, S. S.,
 252 Markon, C. J., Melnikov, E. S., Moskalenko, N. G., Talbot, S. S., Yurtsev, B. A. (†), and Team, T. other members of the C.:
 253 The Circumpolar Arctic vegetation map, *J. Veg. Sci.*, 16, 267–282, <https://doi.org/10.1111/j.1654-1103.2005.tb02365.x>, 2005.
- 254 Wang, J. A., Sulla-Menashe, D., Woodcock, C. E., Sonnentag, O., Keeling, R. F., and Friedl, M. A.: Extensive land cover
 255 change across Arctic–Boreal Northwestern North America from disturbance and climate forcing, *Global Change Biol.*, 26,
 256 807–822, <https://doi.org/10.1111/gcb.14804>, 2020.
- 257 Watts, J. D., Natali, S. M., Minions, C., Risk, D., Arndt, K., Zona, D., Euskirchen, E. S., Rocha, A. V., Sonnentag, O., Helbig,
 258 M., Kalhori, A., Oechel, W., Ikawa, H., Ueyama, M., Suzuki, R., Kobayashi, H., Celis, G., Schuur, E. A. G., Humphreys, E.,
 259 Kim, Y., Lee, B.-Y., Goetz, S., Madani, N., Schiferl, L. D., Commane, R., Kimball, J. S., Liu, Z., Torn, M. S., Potter, S., Wang,
 260 J. A., Jorgenson, M. T., Xiao, J., Li, X., and Edgar, C.: Soil respiration strongly offsets carbon uptake in Alaska and Northwest
 261 Canada, *Environ. Res. Lett.*, 16, 084051, <https://doi.org/10.1088/1748-9326/ac1222>, 2021.
- 262 Yi, Y., Kimball, J. S., Chen, R. H., Moghaddam, M., Reichle, R. H., Mishra, U., Zona, D., and Oechel, W. C.: Characterizing
 263 permafrost active layer dynamics and sensitivity to landscape spatial heterogeneity in Alaska, *Cryosphere*, 12, 145–161,
 264 <https://doi.org/10.5194/tc-12-145-2018>, 2018.

- 265 Yi, Y., Kimball, J. S., Chen, R. H., Moghaddam, M., and Miller, C. E.: Sensitivity of active-layer freezing process to snow
266 cover in Arctic Alaska, *Cryosphere*, 13, 197–218, <https://doi.org/10.5194/tc-13-197-2019>, 2019.
- 267 Zhang, Y., Joiner, J., Alemohammad, S. H., Zhou, S., and Gentine, P.: A global spatially contiguous solar-induced fluorescence
268 (CSIF) dataset using neural networks, *Biogeosciences*, 15, 5779–5800, <https://doi.org/10.5194/bg-15-5779-2018>, 2018.
- 269 Zona, D., Gioli, B., Commane, R., Lindaas, J., Wofsy, S. C., Miller, C. E., Dinardo, S. J., Dengel, S., Sweeney, C., Karion,
270 A., Chang, R. Y.-W., Henderson, J. M., Murphy, P. C., Goodrich, J. P., Moreaux, V., Liljedahl, A., Watts, J. D., Kimball, J.
271 S., Lipson, D. A., and Oechel, W. C.: Cold season emissions dominate the Arctic tundra methane budget, *PNAS*, 113, 40–45,
272 <https://doi.org/10.1073/pnas.1516017113>, 2016.